MATERIALS SCIENCE

Nitrite reductase–mimicking catalysis temporally regulating nitric oxide concentration gradient adaptive for antibacterial therapy

Yonghai Feng[1], Yi Yu[1], Hui Shi[1], Jiaxiang Bai[2], Liangliang Wang[3]*, Tianke Yang[4]*, Lei Liu[1]*

Copyright © 2024 The Authors, some rights reserved; exclusive licensee American Association for the Advancement of Science. No claim to original U.S. Government Works. Distributed under a Creative Commons Attribution NonCommercial License 4.0 (CC BY-NC).

The unique bacterial infection microenvironment (IME) usually requires complicated design of nanomaterials to adapt to IME for enhancing antibacterial therapy. Here, an alternative IME adaptative nitrite reductase–mimicking nanozyme is constructed by in situ growth of ultrasmall copper sulfide clusters on the surface of a nanofibrillar lysozyme assembly (NFLA/CuS NHs), which can temporally regulate nitric oxide (NO) gradient concentration to kill bacteria initially and promote tissue regeneration subsequently. Benefiting from a copper nitrite reductase (CuNIR)–inspired structure with CuS cluster as active center and NFLA as skeleton, NFLA/CuS NHs efficiently boost the catalytic reduction of nitrite to NO. The inherent supramolecular fibrillar networks displays excellent bacterial capture capability, facilitating initial high-concentration NO attacks on the bacteria. The subsequent catalytic release of low-concentration NO by NFLA/CuS NHs–mediated nitrite reduction remarkably promotes cell migration and angiogenesis. This work paves the way for dynamically eliminating MDR bacterial infection and promoting tissue regeneration in a simple and smart way through CuNIR-mimicking catalysis.

INTRODUCTION

Developing efficient antibacterial agents is emergent due to antimicrobial resistance (AMR), which poses a great threat to global health. Notably, bacterial communities at infection sites are complex systems with multiple types of bacteria and a unique metabolic microenvironment, characterized by low pH, local temperature increase, high reactive oxygen species (ROS), specific enzymes, and nutrient deficiency (*1*, *2*). Therefore, an ideal antimicrobial agent should not only exhibit high antimicrobial activity but also have good adaptability to the infection microenvironment (IME) to effectively promote tissue repair.

Antimicrobial nanozymes are enzyme mimics capable of catalyzing endogenous substances to produce highly active antimicrobial factors for efficiently killing bacteria (*3*). However, most current antimicrobial nanozymes are peroxidase or oxidase-like nanomaterials that convert H_2O_2 or O_2 to ROS (e.g., •OH, O_2^-) as antibacterial agents. While ROS has high susceptibility to bacteria, their short life span (<200 ns) and limited diffusion distance (approximately 20 nm) (*4*) require excessive generation to disrupt bacteria, which is also deleterious to normal cells (*5*, *6*) and could trigger the macrophage polarization toward M1 macrophages (proinflammatory) (*7*), hindering tissue repair. Although there are some proposed strategies to construct carriers to contain antimicrobial agents and growing factor to treat the infected wound and wound healing, it is still emergence to develop a simple way to tackle the complicated issues by a smart manner. In comparison, nitric oxide (NO), a diatomic radical with a longer half-life (0.09 to 2 s) (*8*) and enhanced tissue penetration capability, serves as a powerful antibacterial agent (*9*, *10*). It also plays a crucial role in wound healing regulation and tissue regeneration below a threshold of NO concentration (*11*, *12*). Therefore, developing nanozymes with dynamic NO generation as an antimicrobial factor holds promise for achieving efficient antimicrobial activity and tissue repair promotion. However, several key requirements need to meet, such as (i) to select a suitable natural enzyme as the biomimetic model, (ii) to design nanozymes with high enzyme-like activity, and (iii) to facilitate the nanozyme with the adaptability to the IME, for instance, fast generation with high concentration of NO initially for killing bacteria efficiently and adapting to slow generation with low concentration of NO for tissue regeneration.

In nature, nitrite reductases with heme, copper, and molybdenum centers can catalyze the reduction of nitrite (NO_2^-) to NO, playing a crucial role in various physiological and pathological processes, as well as the natural nitrogen cycle (*13*, *14*). Among them, copper-containing nitrite reductase (CuNIR) has an active copper(II) center with $(His)_3$–H_2O ligation, mediating the catalytic reduction of NO_2^- to NO (*15*, *16*), which can be simply summarized as Eqs. 1 and 2 (*11*, *17*–*19*)

$$Cu(II) + e^- \rightarrow Cu(I) \quad (1)$$

$$Cu(I) + NO_2^- + 2H^+ \rightarrow Cu(II) + NO + H_2O \quad (2)$$

However, designing nitrite reductases mimics is highly anticipated but still challenged. Inspired by Fe_3O_4 nanoparticles (NPs) as represented peroxidase-like nanozymes with Fe active centers and the successful mimicking of natural horseradish peroxidase (*3*), we thus envision that Cu(II)-based nanomaterials (e.g., CuO and CuS) might have CuNIR-like properties due to the presence of Cu(II) species, as the mimics of CuNIR. Although the concentration of production (NO) is depended on the concentration of substrate, showing high initially and becoming low with the decrease of substrate, it is still

[1]Institute for Advanced Materials, School of Materials Science and Engineering, Jiangsu University, Zhenjiang 212013, Jiangsu Province, China. [2]Department of Orthopedics, The First Affiliated Hospital of USTC, Division of Life Sciences and Medicine, University of Science and Technology of China, Hefei 230001, Anhui Province, China. [3]Department of Orthopedics, The Affiliated Changzhou Second People's Hospital of Nanjing Medical University, Changzhou 213003, Jiangsu Province, China. [4]Department of Ophthalmology, The First Affiliated Hospital of USTC, Division of Life Sciences and Medicine, University of Science and Technology of China, Hefei 230001, Anhui Province, China.
*Corresponding author. Email: m18862238837@163.com (L.W.); yangtianke@ustc.edu.cn (T.Y.); liul@ujs.edu.cn (L.L.)

challenged to exhibit the dynamic and dramatical difference of NO releasing rate temporally (fast generation with high concentration of NO and slow generation with low concentration of NO) to adapt to the IME for killing bacteria initially and tissue regeneration subsequently.

To meet the requirements of nanozyme design mentioned above, we proposed a strategy to construct CuNIR mimics via biomineralization (*20–23*), which immobilizes the copper-based clusters and integrates the multiply copper active sites by peptide self-assembling, and it can spatially confine and contain abundant surface-active functional groups, further regulate the formation and distribution of ultrasmall NPs. They also involve strong interactions with reaction substrates and good electron transfer properties, akin to a natural enzyme cofactor, which are beneficial for enhancing catalytic activity. In details (Fig. 1A), nanohybrids composed of nanofibrillar lysozyme assembly (NFLA) confining ultrasmall copper sulfide NPs (NFLA/CuS NHs) were fabricated as smart and highly efficient CuNIR mimics. The ultrasmall CuS NPs with more exposed active sites are designed to mimic the active copper(II) centers of CuNIR. Lysozyme fibrils with more amino acids exposed can be chelated with copper (II), mimicking the spatial structure of CuNIR. Moreover, the nanozymes with the mobilization of ultrasmall CuS NPs onto the NFLA might be superior to the natural CuNIR, due to multiply protected and stabilized active centers in the nanozyme. Furthermore, the "cofactor-like" effect of NFLA facilitating substrate [nitrite and ascorbic acid (AA)] adsorption on NFLA/CuS NHs synergistically enhances the CuNIR-like activity, which was both verified in experiments and theoretical simulations. We have successfully achieved temporal regulation of NO concentration gradients dynamically and markedly through precise control of enzymatic catalysis kinetics by the proposed specific structure. It allows for a high concentration of NO during the initial stages of catalysis, ensuring its efficacy in

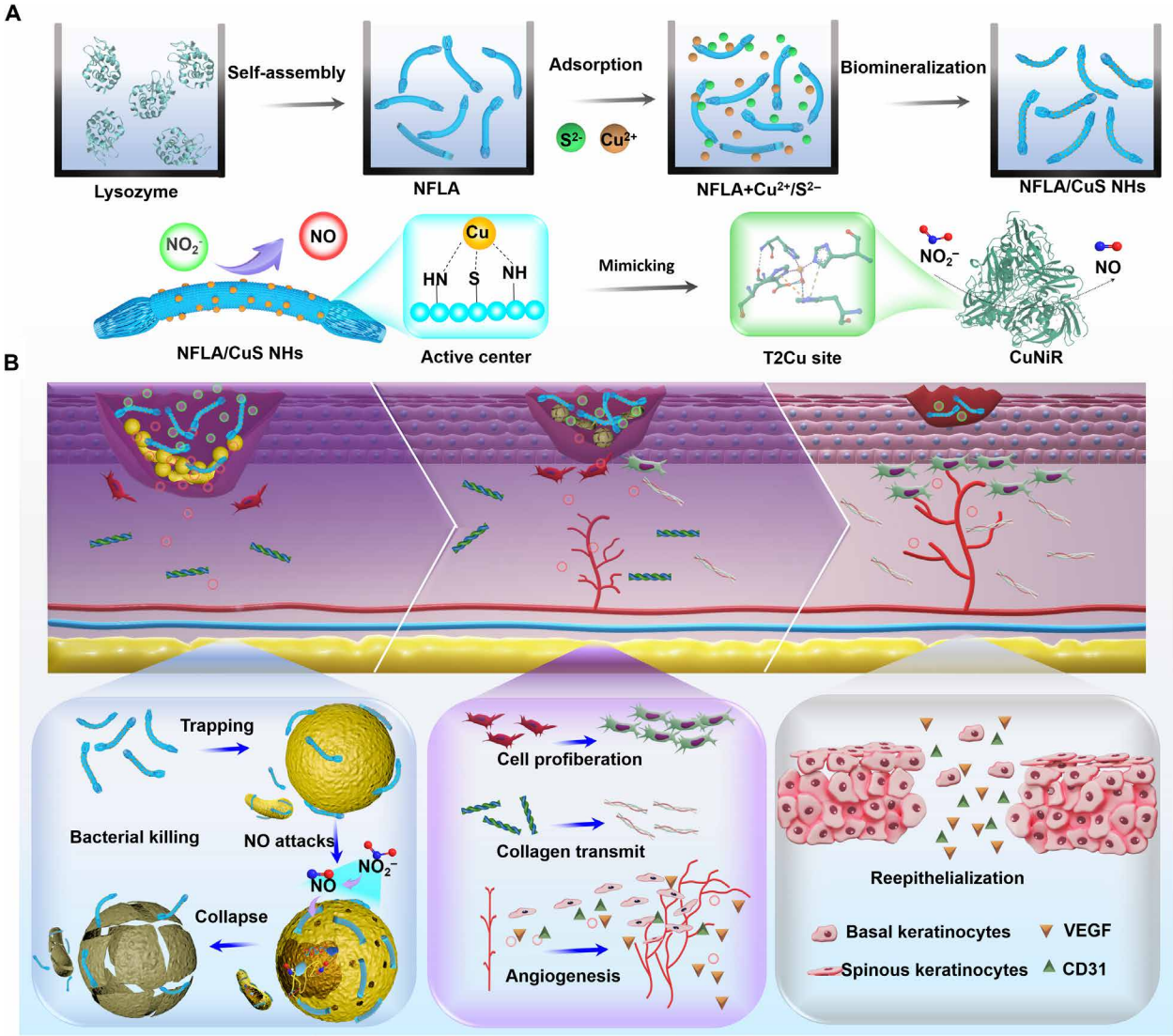

Fig. 1. Schematic illustration of NFLA/CuS NHs preparation and antibacterial mechanism and tissue repair. (**A**) Synthesis of NFLA/CuS NHs with CuNiR-like activity for catalyzing the conversion of NO_2^- to NO. (**B**) Mechanism of antibacterial therapy involving NFLA/CuS NH-based CuNiR mimetic catalysis by temporal regulation of the nitrite oxide concentration gradient.

antimicrobial action. Subsequently, there is a sustained release of NO at lower concentrations in the later stages, contributing to the facilitation and promotion of tissue repair (Fig. 1B). This work paves the way for eliminating MDR bacterial infection and promoting tissue regeneration in a simple and smart way through CuNIR-mimicking catalysis to adapt the IME dynamically.

RESULTS

Synthesis and characterizations of NFLA/CuS NHs

The NFLA/CuS NHs were fabricated through a biomineralization-inspired strategy, confining ultrasmall metal/metal oxide NPs on the biotemplates (Fig. 1A). Fibrillar lysozyme assemblies (NFLAs) with an average diameter of ca. 14.9 nm and a length of greater than 1 μm (figs. S1A and S2A) were first prepared by the deep eutectic solvent method, and these assemblies were subsequently redispersed in water and incubated with Cu^{2+} ions. After reacting with Na_2S, an alternative nanohybrid of NFLA confining ultrasmall CuS NPs (NFLA/CuS NHs) was obtained. Both the transmission electron microscopy (TEM) bright-field and dark-field images (Fig. 2, A and B) show that the NFLA/CuS NHs have one-dimensional (1D) nanofiber-like structures with ultrasmall CuS NPs (dark dots in Fig. 2A or bright dots in Fig. 2B) orderly allied and dispersed on the NFLA surfaces. The CuS/NFLA ratio substantially affects the particle size of CuS NPs. When the CuS/NFLA ratios are of 0.5:1 and 1:1, the average particle size of CuS NPs is less than 4.4 nm (fig. S1, B and C). However, increasing the CuS loading on NFLA (CuS/NFLA = 3:1) not only causes the formation of larger-sized CuS NPs (ca. 7.7 nm) but also induces the obvious aggregation of NFLA (fig. S1D). As distinguished by the aberration-corrected high-angle annular dark-field scanning TEM (AC-HAADF-STEM) images (Fig. 2C and fig. S3), a large number of bright dots circled by red color are observed on the nanohybrid surfaces, attributed to the exposed Cu atoms. In addition, the ultrafine NPs are dominant single-crystalline structures with lattice spacings

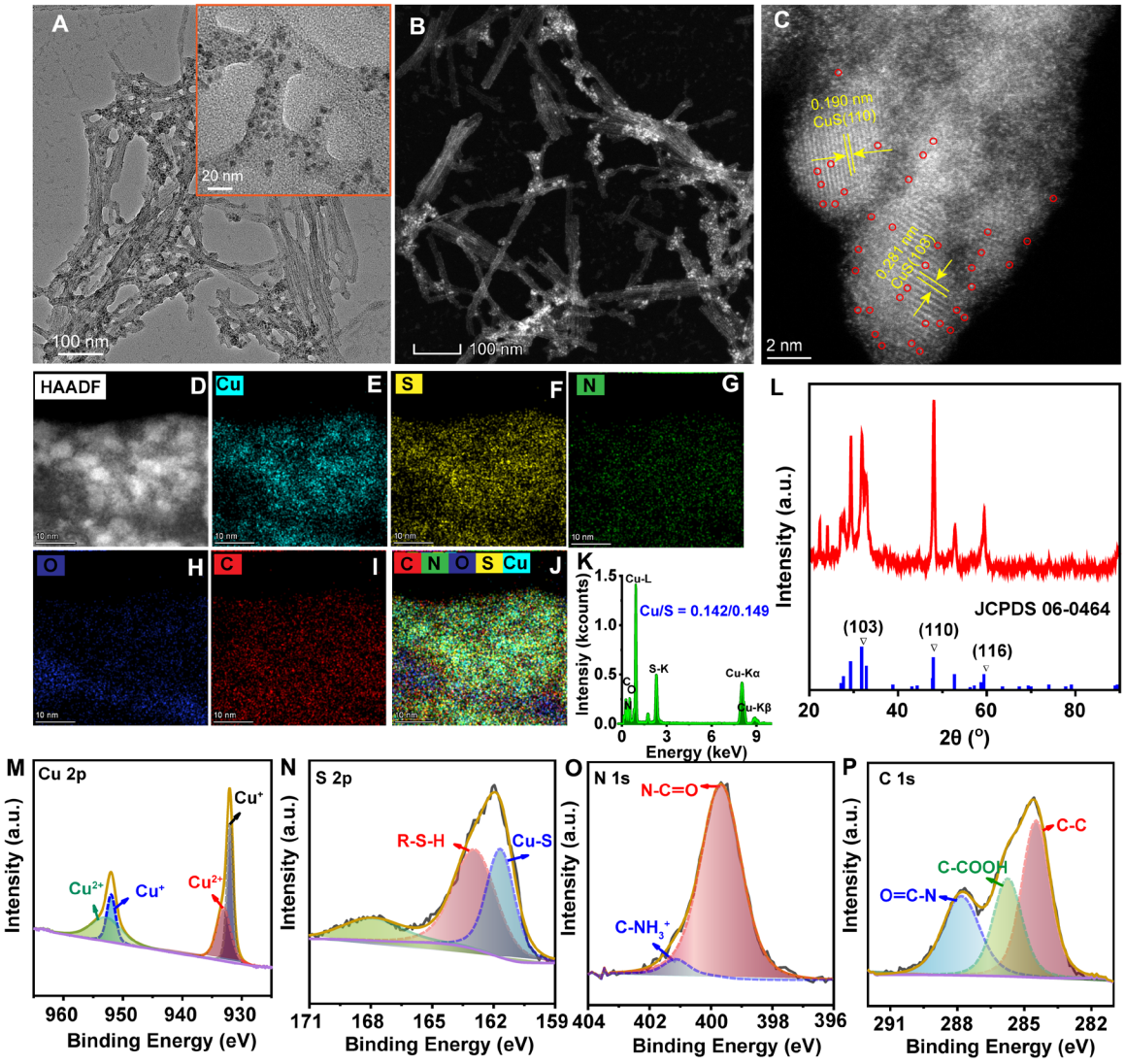

Fig. 2. Morphology and structure of NFLA/CuS NHs. (**A**) TEM bright-field image of NFLA/CuS NHs. The inset is the corresponding enlarged TEM image. (**B**) TEM dark-field image of NFLA/CuS NHs. (**C**) High resolution STEM image of NFLA/CuS NHs. (**D** to **K**) HAADF-STEM image of NFLA/CuS NHs and the corresponding Cu, S, N, O, and C distributions. (**L**) XRD pattern of NFLA/CuS NHs. (**M** to **P**) Cu 2p, S 2p, N 1 s, and C 1 s XPS spectra of NFLA/CuS NHs.

of ca. 0.281 or 0.19 nm, similar to those of the (103) and (110) planes of copper sulfide, respectively. The HAADF-STEM image (Fig. 2D) and the corresponding energy-dispersive x-ray (EDX) elemental mappings of Cu and S (Fig. 2, E and F) demonstrate similar distributions, while the mappings of N, O, and C (Fig. 2, G to I) are homogeneously distributed in the selected region. However, their good merging (Fig. 2J) further reveals that CuS NPs are orderly and evenly formed on the NFLA surfaces. Notably, the EDX spectrum (Fig. 2K) shows that the ratio of S species is slightly greater than that of Cu species, mainly due to the presence of sulfur in the lysozyme nanofibers. The actual Cu content in the NFLA/CuS NHs is approximately 30 weight %, according to the inductively coupled plasma–optical emission spectrometry (ICP-OES) (table S1). In the x-ray diffraction (XRD) pattern (Fig. 2L), typical crystalline peaks of CuS NPs with much stronger intensities at the (103) and (110) planes are presented, which is in line with the high-resolution STEM result (Fig. 2C). The binding states of Cu detected by x-ray photoelectron spectroscopy (XPS) reveal the coexistence of Cu^{2+} and Cu^{+} (Fig. 2M), while the XPS spectrum of S 2p (Fig. 2N) demonstrates that in addition to the Cu—S bond, thiol groups (R-S-H) are also present in NFLA/CuS NHs (consistent with the EDX analysis). Both the N 1s and C 1s XPS spectra display the presence of NH_3^+, N—C═O, and C—COOH groups (Fig. 2, O and P), which can serve as anchoring sites for Cu^{2+} ions to stabilize ultrasmall CuS NPs on the surfaces of NFLA/CuS NHs. In addition, it is found that NFLA/CuS NHs could maintain a robust fiber network structure and a relatively narrow size distribution when dispersed in aqueous solutions across different pH (5.5 to 8.5) (fig. S2, C to J). Even after 2 weeks of storage, they retained their original morphology and favorable physicochemical properties (fig. S4). Furthermore, NFLA/CuS NHs exhibited strong optical absorption in the NIR region [fig. S5A; the ultraviolet-visible (UV-vis) spectra], suggesting the promising 980-nm responsive photothermal activity (fig. S5, B and C) with a photothermal conversion efficiency of 30.7% (fig. S5, D and E). It can be an excellent photothermal agent for photothermal therapy (PTT).

CuNIR-mimicking activities of NFLA/CuS NHs

The *N*-(1-naphthyl)-ethylenediamine dihydrochloride (NED) colorimetric method was used to detect the concentration of NO_2^- during the CuNIR-mimetic reaction. Initially, NO_2^- reacts with 4-aminobenzenesulfonic acid through diazotization, subsequently coupling with NED to produce a distinct purple color (see inset in Fig. 3A). Furthermore, UV-vis absorption spectra illustrate a linear decrease in the intensity of the characteristic peak at 544 nm with declining NO_2^- concentrations (Fig. 3A), facilitating the quantitative determination of NO_2^- before and after the reaction, and reflecting the generated NO concentration indirectly. The generation of NO was further confirmed by its special colorimetric reaction with $FeSO_4$ (*24*), resulting in the formation of brown $Fe(NO)SO_4$ (fig. S6). In addition, electron paramagnetic resonance (EPR) spectra, using 2-phenyl-4,4,5,5-tetramethyl-imidazoline-1-oxyl 3-oxide (PTIO) as the spin-trapping agent, unequivocally demonstrates the catalytic release of NO radical (Fig. 3B) (*25*). Notably, only a minimal amount of spontaneous NO release is observed in AA + NO_2^- without NFLA/CuS NHs.

Figure 3C reveals the catalytic potential of several commercial Cu-based materials—such as $CuCl_2$, Cu, CuO, Cu_2O, and CuS—in reducing NO_2^- to NO. The NO_2^- conversion at 20 min follows the order of $CuCl_2$ (72%) ≫ CuS (46.6%) > CuO (43.1%) ≫ Cu_2O (32.4%) ≫ Cu (20.4%) (Fig. 3D), indicating that homogeneous and soluble $CuCl_2$ exhibits the highest activity due to maximal utilization efficiency of active Cu(II) sites in aqueous solution. Conversely, solid CuS and CuO with exposed Cu(II) sites demonstrate superior activity compared to Cu_2O, primarily due to their facile generation of protons (H^+) via AA reduction. Although CuS exhibits higher NO_2^- conversion than CuO, it remains substantially lower than $CuCl_2$. Consequently, a nanostructure of NFLA/CuS NHs was fabricated as a highly efficient CuNIR mimic, yielding a NO_2^- conversion of 61.9%. Despite a slightly lower NO_2^- conversion, NFLA/CuS NHs boast a turnover frequency (TOF) based on Cu content that is approximately twice as high as $CuCl_2$ and 5.5 times greater than pure CuS (Fig. 3D and table S1), underscoring their remarkable catalytic efficacy.

The catalytic properties of NFLA/CuS NHs were further elucidated through Michaelis-Menten kinetics (Fig. 3, E and F). The calculated kinetic parameters (listed in table S2) demonstrate that among solid CuNIR mimics (CuO, CuS, and NFLA/CuS NHs), NFLA/CuS NHs exhibit the lowest Michaelis constant (K_m) (31.4 mM) when NO_2^- serves as the substrate, even surpassing that of $CuCl_2$, indicating superior affinity for NO_2^-. In addition, when AA is used as the substrate, NFLA/CuS NHs display a lower K_m value (approximately 2.2 mM) and larger V_{max} (3.0×10^{-8} M s^{-1}), signifying stronger AA binding affinity and greater catalytic performance compared to CuO and CuS. Pure NFLA (CuS/NFLA = 0) exhibits no catalytic activity (Fig. 3G). Increasing the CuS/NFLA ratio from 0.5 to 6 enhances the NO_2^- conversion from 30.7 to 70.8%, confirming CuS as the active component. However, high CuS loading on NFLA/CuS NHs (e.g., CuS/NFLA = 3, 6) results in elevated NO_2^- conversion but diminished TOF (inset in Fig. 3G), indicating reduced activity. Furthermore, NO_2^- conversion notably depends on AA concentration (fig. S7), with sufficient AA (10 mM) maintaining NO_2^- conversion at approximately 80% across a range of NO_2^- concentrations (2.5 to 10 mM) (fig. S8). Moreover, increasing the NFLA/CuS NHs concentration also favors a substantial enhancement in NO_2^- conversion (fig. S9) due to more available active copper sites for accelerating the reduction of NO_2^- to NO. As depicted by Eqs. 1 to 2, the catalytic activity of NFLA/CuS NHs is also influenced by the pH of solution (Fig. 3H). Within the pH range of 3 to 8, maximum catalytic activity occurs at pH 5, approximately twice as high as at pH 7.0. Overall, a weakly acidic environment facilitates reduction owing to the presence of sufficient H^+. Furthermore, increasing reaction temperature promotes NO_2^- conversion (fig. S10). Consequently, when exposed to an NIR stimulus (980-nm laser, 0.8 W cm^{-2}) for 10 min, NFLA/CuS NHs exhibit a ca. 30% decrease in the maximum absorption peak at 544 nm (Fig. 3I) due to the heating effect, resulting in a final NO_2^- conversion comparable to that of $CuCl_2$ (Fig. 3D).

Furthermore, a dynamic and notable difference in NO release rate over time is observed with NFLA/CuS NHs. Figure 3J illustrates the relationship between NO_2^- conversion and the corresponding average release rate of NO over time. Within the initial 0.5 hours, NO_2^- conversion reaches around 60% (at 0.5 hours), with a high average release rate of NO at 120 μmol $hour^{-1}$. However, with prolonged reaction time, in the subsequent half-hour (at 1 hour), the increased NO_2^- conversion is only 6%, accompanied by a sharp decrease in the average release rate of NO to 12 μmol $hour^{-1}$. As the reaction progresses for an additional hour (at 2 hours), both the increased NO_2^- conversion rate and NO average release rate further

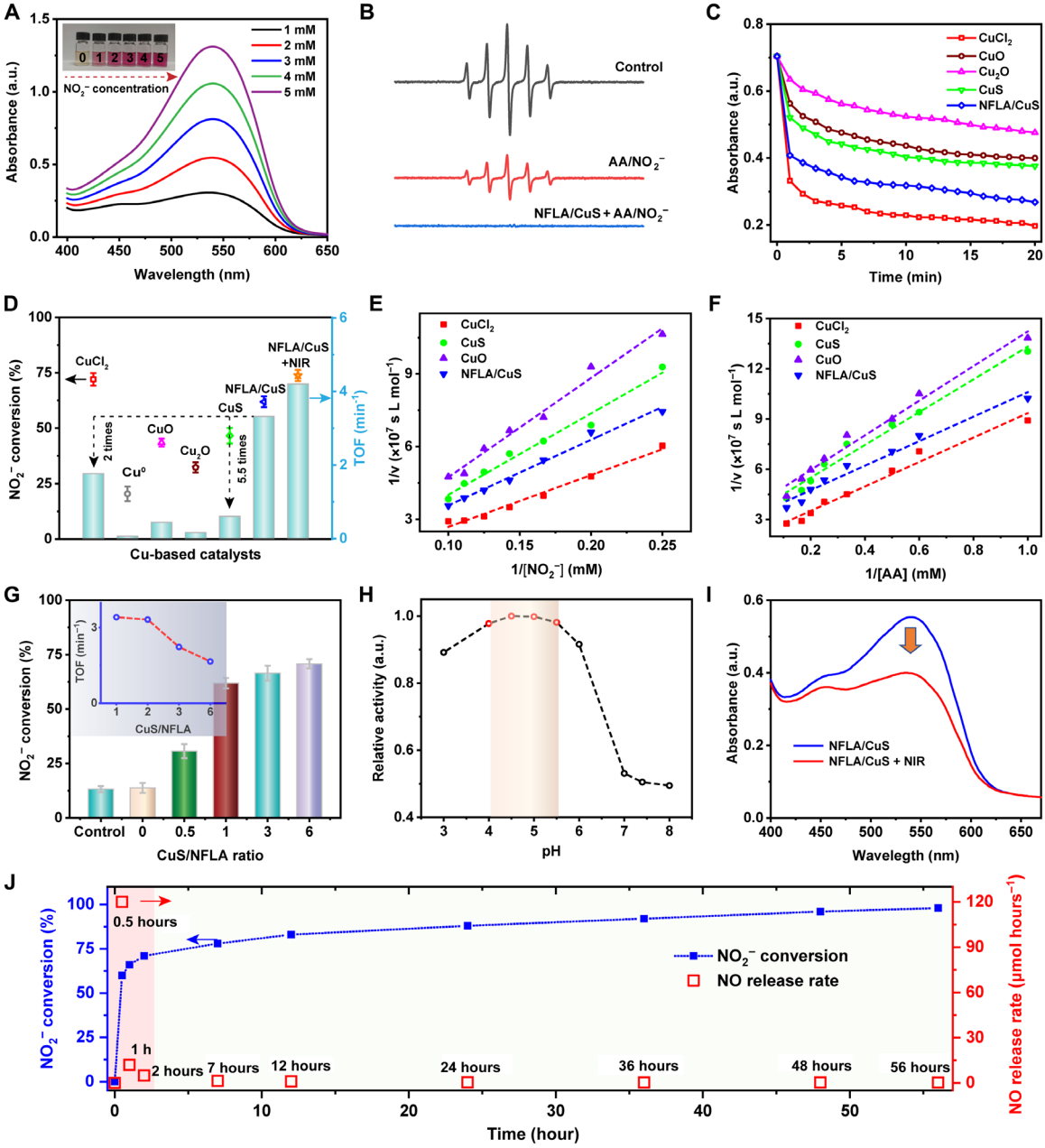

Fig. 3. Catalytic performance of NFLA/CuS NHs for NO_2^- reduction. (**A**) UV-vis absorption spectra of NO_2^- at different concentrations with chromogenic agents. The inset shows the photograph of chromogenic solutions with different NO_2^- concentrations. (**B**) EPR spectra of NO radicals generated by NO_2^- reduction. (**C**) Changes in nitrite absorbance with time over different Cu-based catalysts. (**D**) NO_2^- conversion and TOF for different copper-based catalysts. The TOF is calculated at initial reaction time of 1 min and based on the copper amount of all the catalysts by following the equation of TOF = Converted nitrite (mol)/Copper content in catalysts (mol)/Reaction time (min). (**E**) Double-reciprocal plots for determining the kinetic constants for the NO_2^- substrate. (**F**) Double-reciprocal plots for determining the kinetic constants for the AA substrate. (**G**) Effect of CuS/NFLA ratio on the NO_2^- conversion. (**H**) Relative activity at different pH values. (**I**) UV absorption spectrum of nitrite after the reaction over NFLA/CuS NHs without and with NIR irradiation. (**J**) Variation of NO_2^- conversion and NO release rate with respect to reaction time.

decrease to 5% and 5 μmol $hour^{-1}$, respectively. Despite this, catalytic conversion of NO_2^- continues slowly over the following 54 hours until reaching 100%, while the NO release rate further decreases, not exceeding 1 μmol $hour^{-1}$. The findings suggest the feasibility of achieving temporal control over NO release concentration by mimicking the nitrate reductase reaction. During the initial short period (e.g., 0.5 hours), the catalytic system can efficiently release relatively high concentrations of NO. In contrast, during the subsequent extended period (e.g., 54 hours), a gradual release of lower concentrations of NO is observed. This strategic temporal modulation aims to achieve a dual-purpose effect, the effective provision of potent antibacterial properties during the initial phase, followed by the facilitation of tissue repair through the controlled release of NO dynamically and markedly.

Proposed mechanism of NFLA/CuS NHs enhancing catalytic NO_2^- reduction

The CuNIR enzyme is believed to operate through a five-step pathway for catalyzing the reduction of NO_2^- to NO (*26*), as depicted in fig. S11. As a bioinspired CuNIR mimic, the NFLA/CuS NHs may follow a similar catalytic mechanism (*27*). The exposed CuS (103) planes on the surface of NFLA/CuS NHs are suggested to be the active sites for activating NO_2^- reduction. Thus, density functional theory (DFT) calculations were performed to illustrate the proposed mechanism and reaction energy diagram on the CuS (103) plane and the CuO (111) plane for comparison (Fig. 4A). Initially, NO_2^- is expected to bind to the active Cu(II) site of the CuS(103) plane, forming a complex known as nitrite-bound Cu(II) center (Cu^{II}-NO_2). This process is spontaneous and exothermic, with an adsorption energy of −1.1 eV. Subsequently, the Cu^{II}-NO_2 complex is reduced to a nitrite-bound Cu(I) center complex (Cu^{I}-NO_2) by AA, an endothermic reaction that could potentially serve as the rate-determining step due to its higher energy requirement (0.8 eV)

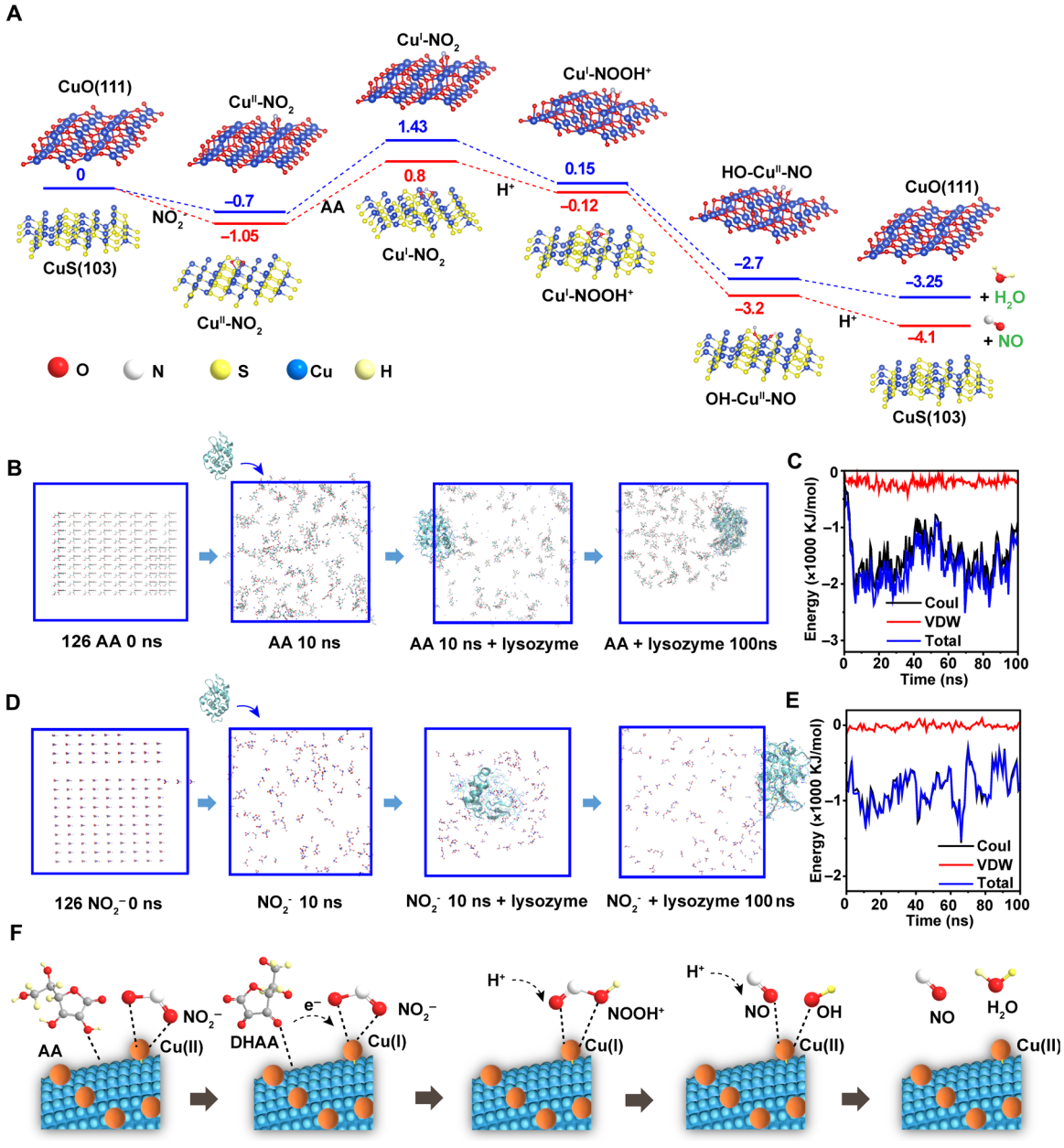

Fig. 4. Proposed mechanism for the reduction of NO_2^- to NO over NFLA/CuS NHs in presence of AA. (**A**) Possible reaction pathway and corresponding energy diagram for the reduction of NO_2^- to NO catalyzed by the CuS (103) plane and Cu (111) plane. The relative energies are expressed in eV. (**B**) Schematic diagram of the MD simulation for the interaction between lysozyme and AA. (**C**) Diagrams of the interaction energy variation over time for lysozyme binding to AA. (**D**) Schematic diagram of the MD simulation for the interaction between lysozyme and nitrite. (**E**) Diagrams of the interaction energy variation over time for lysozyme binding nitrite. Mole ratio of lysozyme to AA or nitrite molecules is 1/126. (**F**) Proposed mechanism scheme of the catalytic reduction of NO_2^- to NO by NFLA/CuS NHs in the presence of AA.

compared to other steps. Upon proton (H^+) transfer, Cu^I-NO_2 may further convert into the Cu^I-$NOOH^+$ intermediate, which is susceptible to N—O bound scission, resulting in the formation of an intermediate composed of nitric oxide and hydroxide-bound Cu(I) center (NO-Cu^{II}-OH). Last, NO is liberated from the NO-Cu^{II}-OH intermediate after another H^+ transfer, accompanied by the loss of H_2O and the regeneration of the original Cu(II) center. Compared to CuO, CuS exhibits superior adsorption of NO_2^- and a lower energy barrier (0.8 eV versus 1.43 eV), leading to enhance NO production during the catalytic reduction of NO_2^-. In addition, NIR irradiation remarkably promotes the NO_2^- conversion to NO, possibly due to the local hyperthermia generated by CuS, which facilitates the breakdown of the energy barrier of Cu^{II}-NO_2 → Cu^I-NO_2.

Furthermore, the excellent substrate affinity with NFLA may also contribute to the enhanced catalytic activity compared to pure CuS. Amyloid peptide assemblies could function as "cofactors" for enzymes, promoting catalyst activity by virtue of their strong interactions with substrates (*21*, *28*), such as NO_2^- and AA (fig. S12). Molecular dynamic (MD) simulation (Fig. 4, B to E) was used to assess the interaction between lysozyme and nitrite, as well as AA molecules, reflecting the real reaction system. After 100 ns, the two calculation systems reached equilibrium (fig. S13), with several AA molecules bound by the lysozyme molecule (Fig. 4B) via hydrogen bonds (fig. S14). A similar phenomenon was observed for the nitrite substrate system (Fig. 4, D and E). Notably, the interaction between lysozyme and AA is considerably stronger than that between lysozyme and nitrite, indicating the superior affinity of lysozyme with AA. This affinity is crucial for accelerating the reduction of Cu(II) to Cu(I) and the production of protons, ultimately facilitating the reduction of NO_2^- to NO by the NFLA/CuS nanozyme. In summary, the intrinsic CuNIR-like activity of CuS clusters and the cofactor-like effect of NFLA synergistically contribute to the enhanced catalytic activity, following a CuNIR-mimicking reaction pathway (Fig. 4F).

Catalytic antibacterial performance of NFLA/CuS NHs

The catalytic antibacterial efficacy of NFLA/CuS NHs against both Gram-negative *Escherichia coli* (*E. coli*) and Gram-positive methicillin-resistant *Staphylococcus aureus* (MRSA) was evaluated across six experimental groups: (I) control (buffer), (II) NFLA/CuS, (III) AA/NO_2^-, (IV) AA/NO_2^- + NFLA/CuS, (V) NFLA/CuS + NIR, (VI) NFLA/CuS + AA/NO_2^- + NIR. Fig. 5, A to D depicts bacterial colony diagrams and fluorescence images of *E. coli* and MRSA following various treatments, alongside corresponding bacterial viabilities. Compared to the control group, both *E. coli* and MRSA exhibited viabilities exceeding 90% when treated with NFLA/CuS NHs or AA/NO_2^- alone for 10 min. However, their viabilities dramatically decreased to 23.0 and 34.8%, respectively, when exposed to AA/NO_2^- + NFLA/CuS, which was attributable to the intrinsic antibacterial activity of NO released from the catalytic reduction of NO_2^- over NFLA/CuS. Moreover, NIR irradiation (980 nm laser irradiation at 0.8 W cm^{-2} for 10 min) notably enhanced NO_2^- conversion to NO, thereby accelerating bacterial eradication due to the rapid initial release of NO (refer to Fig. 3I). Consequently, viability plummeted nearly to zero after treatment with NFLA/CuS + AA/NO_2^- + NIR, primarily due to intensify NO release coupled with mild PTT. However, in group treated with single PTT (group V), the viabilities of *E. coli* and MRSA were only 50.6 and 55.4%, respectively, likely due to inadequate heat generation (45°C). Thus, the excellent bacteria eradiation is ascribed to the combination of PTT and enhanced efficiency of generated NO under locally heating by NIR. It is noteworthy that MRSA is a typical drug-resistant bacteria, displaying a strong resistance to oxacillin and clarithromycin (fig. S15). However, it is obvious that they hardly survive when treated with NFLA/CuS NHs in the presence of NO_2^- and AA under NIR irradiation. This indicates that the nitrite reductase–mimicking catalysis over NFLA/CuS NHs can be an effective antibiotic-free strategy for eliminating drug-resistant bacteria.

Catalytic antibacterial mechanism of NFLA/CuS NHs

Bacterial capture

The long, fine, and flexible structure of biomimetic nanofibrous peptide assemblies facilitates effective entrapment of bacteria, as demonstrated in previous studies (*29*) and observed for NFLA (fig. S16). In addition, NFLA/CuS NHs demonstrated notable bacterial entrapment, leading to a notable increase in the fluorescence signals of *E. coli* and MRSA, as depicted in fluorescence images [Fig. 5A (group II) and Fig. 5C (group II)], owing to bacterial agglutination. Scanning electron microscopy (SEM) images [Fig. 5E (group II) and Fig. 5F (group II)] illustrate that *E. coli* and MRSA are fully enveloped by the fibrous network of NFLA/CuS NHs, which is in line with the TEM images (fig. S17). The zeta potentials of NFLA/CuS NHs in aqueous solutions with pH values of 5.5, 7.0, and 8.5 are all negatively charged (fig. S18). Notably, in neutral aqueous solution, the zeta potential value is similar to that of *E. coli* and MRSA, resulting in little change when NFLA/CuS NHs interact with bacteria (fig. S18). This indicates that the strong bacterial trapping ability of NFLA/CuS NHs is due to their unique structure of lysozyme with multiply interaction among the amino acids exposed outside of lysozyme fibrils. Short-term trapping (10 min) may not markedly inhibit bacterial proliferation, it plays a crucial role in facilitating the localization of the nanozyme and initiating catalytic attacks specifically on bacteria rather than on normal tissues. However, extending the trapping duration beyond 1 hour resulted in a notable decrease in bacterial viability (fig. S19), indicating the potent inhibitory effect of NFLA/CuS NHs on bacterial growth.

Membrane damage

SEM images of bacteria treated with NFLA/CuS NHs under various conditions revealed significant differences (Fig. 5, E and F). Healthy *E. coli* and MRSA (group I) exhibited intact cell membranes with smooth surfaces. Following treatment with NFLA/CuS NHs (group II), bacterial surfaces are ensconced by fibrous networks. However, upon exposure to NO (group IV), bacterial surfaces exhibit roughness and wrinkles despite maintaining integrity. Moderate NIR treatment alone (group V) had a minimal effect on bacterial cell membranes, but when combined with catalytic reaction (group VI), it induced pronounced surface deformations, indicating severe alterations in both *E. coli* and MRSA. TEM images of MRSA further elucidated the extensive deformation (Fig. 5G). Short-term NO treatment (5 and 10 min) yields little discernible difference in MRSA cell membranes compared to the control group, with outlines remaining clear (fig. S20). However, after 15 min of catalytic NO attack, membrane breakdown became evident, consistent with the SEM results (fig. S21). In contrast, PTT treatment results in notable deformations of entire bacteria under higher laser power density (1.0 W cm^{-2}), highlighting distinct mechanisms of bacterial eradication between catalytic NO attack and PTT (fig. S22). When combined, PTT-generated heat enhances catalytic NO release and accelerates NO diffusion into bacterial interiors (Fig. 5, H and I), leading to oxidative and nitrosative damage to membrane lipids and

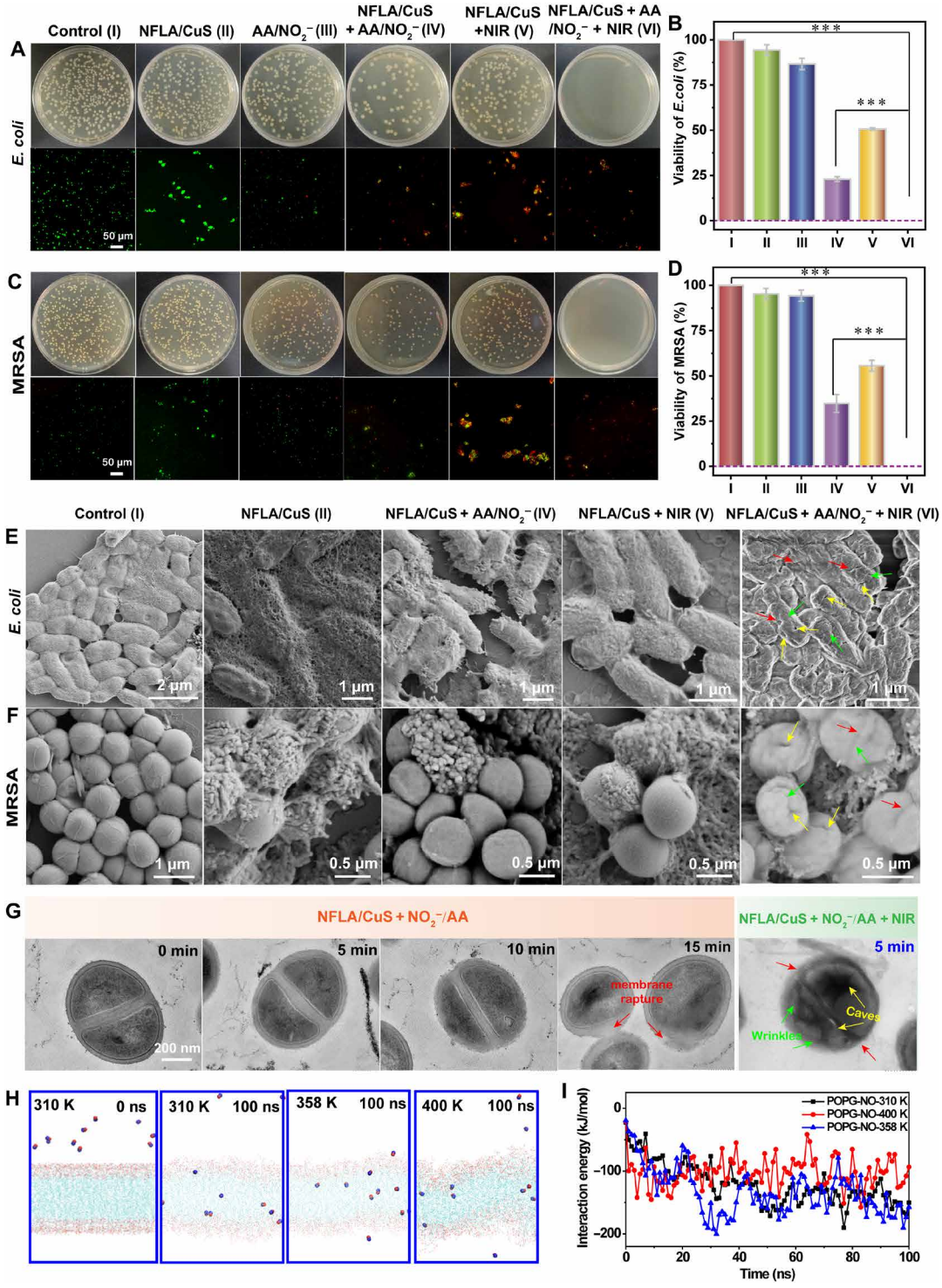

Fig. 5. The antibacterial activity with different treatments. (**A**) Colony diagram of *E. coli* under different treatment conditions and the corresponding fluorescence staining diagram of live dead bacteria. (**B**) Colony diagram of MRSA under different treatment conditions and the corresponding fluorescence staining diagram of live dead bacteria. (**C**) Survival rate of *E. coli* under different treatment conditions. (**D**) Survival rate of MRSA under different treatment conditions. (**E**) SEM images of *E. coli* under different treatment conditions. (**F**) SEM images of MRSA under different treatment conditions. The different treatment conditions used were as follows: control group (I), NFLA/CuS group (II), AA/NO_2^- group (III), NFLA/CuS + AA/NO_2^- group (IV), NFLA/CuS + NIR group (V), and NFLA/CuS + AA/NO_2^- + NIR group (VI). (**G**) TEM images of MRSA under the treatment of NFLA/CuS + AA/NO_2^- or NFLA/CuS + AA/NO_2^- + NIR for different times. (**H**) Schematic diagram of the MD simulation for the interaction between bacterial membrane and NO under different temperature. (**I**) Corresponding diagrams of the interaction energy variation over time. ($n = 6$; ***$P < 0.001$).

even intracellular substances (e.g., proteins and RNA). The intracellular ROS levels of *E. coli* and MRSA were also measured following various treatments, including phosphate-buffered saline (PBS), AA/NO_2^-, NFLA/CuS, NFLA/CuS + AA/NO_2^-, and NFLA/CuS + AA/NO_2^- + NIR. The results indicate that the intracellular ROS levels remained nearly unchanged before and after NFLA/CuS NH-based antibacterial treatments (fig. S23). This suggests that NFLA/CuS NH-based nitrite reductase–mimicking catalysis does not affect the intracellular ROS levels of bacteria but can induce membrane damage directly through generated NO attacks.

Intracellular interference

To investigate the impact of catalytic NO attacks on bacterial interiors, transcriptome analysis was conducted on MRSA subjected to treatments with PBS or NFLA/CuS + NO_2^- + AA based on differential gene expressions (DEGs). Among the nearly 2726 genes examined, 684 were up-regulated, while 585 were down-regulated in the NFLA/CuS + NO_2^- + AA group compared to the control group (Fig. 6A). Cluster analysis of the top 20 up-regulated and down-regulated genes highlighted significant pathways (Fig. 6B). Up-regulated genes such as dppE, yhfL, and dppC, which are associated with quorum sensing and β-lactam resistance, suggest that MRSA adapts to environmental stresses through an underlying transcriptional regulatory network (*30*, *31*), which can be induced by NFLA/CuS + NO_2^- + AA treatment, involving oxidative stress, pH variation, and upregulation of copper ion concentration. Moreover, genes linked to amino acid biosynthesis, such as hom and dapA, indicate intracellular amino acid deficiency, hindering bacterial accumulation and biofilm formation. This is because amino acids for bacterial growth are acquired from extracellular environment rather than from bacterial synthesis (*32*, *33*). Several down-regulated genes related to the cell cycle and cell wall organization—such as femB, mraY, murD, murC, murA1, SAR1252, tig, and BSU29810—suggested impaired bacterial proliferation. This is further supported by the down-regulation of gene clusters (SAOUHSC_01232, purk, and SAR1347), associated with ribosome function and purine metabolism, respectively, which are essential for protein synthesis and nucleic acid function necessary for bacterial growth. Gene Ontology (GO) and Kyoto Encyclopedia of Genes and Genome (KEGG) enrichment analyses (Fig. 6, C to F) revealed the up-regulation of pathways involved in citrate cycle and glyoxylate and dicarboxylate metabolism, which are important for fueling the production of surface and secreted proteins for oxidant clearance (*34*, *35*), further demonstrating the influence of NO attacks. Genes associated with copper ion binding (copA, qoxB, and qoxA) were significantly up-regulated, indicating the strong bacterial binding of NFLA/CuS NHs. Moreover, genes associated with iron-sulfur cluster assembly (sufD, iscU, and sufB) were down-regulated, suggesting that the inhibition of Fe-S cluster assembly is critical for virulence regulation and metabolism in *S. aureus* (*36*, *37*).

Overall, because of their intrinsic bacterial binding, CuNIR-mimicking activity, and NIR responsiveness, NFLA/CuS NHs generate ample NO surrounding bacteria. This exacerbates cell membrane collapse and deformation while inducing intracellular interference, ultimately leading to bacterial death and reduced AMR.

In vitro cytocompatibility and hemocompatibility of NFLA/CuS NHs

Biocompatibility serves as the fundamental criterion for assessing antimicrobial materials intended for biomedical applications. In this study, we conducted a hemolysis assay to evaluate the hemocompatibility of NFLA/CuS NHs. As depicted in Fig. 7 (A and B), the relative hemolysis rate of all the tested groups, which did not exceed 200 μg ml^{-1}, was remarkably lower (≤3%) than that of the positive control group (Triton X-100). This value falls well below the 5% allowable limit for biomaterials. Consequently, a NFLA/CuS NH concentration of 200 μg ml^{-1} was selected for subsequent in vitro studies. Furthermore, we performed a Cell Counting Kit-8 (CCK-8) assay to assess the cytotoxicity of prepared NFLA/CuS NHs toward human umbilical cord endothelial cells (HUVECs) and mouse embryonic fibroblast (NIH-3 T3) cells (Fig. 7, C and E), which are primary cell models involved in wound tissue repair and healing. After 48 hours of incubation with NFLA/CuS NHs at concentrations ranging from 0 to 200 μg ml^{-1}, cell viability exceeded 90% in both cell types, with no significant difference observed among the groups. These findings were further corroborated by LIVE/DEAD staining tests (Fig. 7, D and F), demonstrating the nontoxic nature and biocompatibility of the NFLA/CuS NHs.

Angiogenic effects of NFLA/CuS NHs catalyzing the reduction of nitrite

To enhance cell migration and angiogenesis for effective wound healing, the precise modulation of the NO concentration released from the reduction of NO_2^- catalyzed by NFLA/CuS NHs is crucial. The optimal range for promoting NO release typically lies within a rate of 2 to 8×10^{-10} mol min^{-1} (*38*, *39*). Consequently, in vitro cell migration and scratch assays were conducted to evaluate cell behavior under NFLA/CuS NHs catalysis. Visual inspection and analysis of fixed and stained migrated cells revealed the following order of cell migration ability: (I) PBS ≈ (II) NFLA/CuS ≈ (III) AA/NO_2^- < (V) NFLA/CuS + NIR ≈ (VI) NFLA/CuS + AA/NO_2^- + NIR < (IV) NFLA/CuS + AA/NO_2^- (Fig. 7, G and I). This suggests that NFLA/CuS promotes HUVECs migration in the presence of substrate AA and sodium nitrite. However, migration decreases upon NIR irradiation (NFLA/CuS + AA/NO_2^- + NIR), possibly due to the rapid production of a large amount of NO slightly inhibiting cell migration. Similarly, the scratch assay results exhibited a comparable trend (Fig. 7H), with the cell migration rate calculated for group IV within 24 hours reaching 51.2%, surpassing that of other groups (Fig. 7K). These findings demonstrate that the low concentration of NO catalytically released by NFLA/CuS NHs promotes cell migration. In addition, NFLA/CuS NHs exhibited a noticeable pro-angiogenic ability in the presence of catalytic substrates (AA/NO_2^-). However, the tube-forming ability slightly decreased under NIR light administration, indicating that a moderate concentration of NO fosters pro-angiogenesis (Fig. 7, G and J).

Antibacterial evaluation in an MRSA-infected rat model

Encouraged by the temporal regulation of NO release based on CuNIR-mimicking catalysis over NFLA/CuS NHs, a chronic wound model was established with MRSA as model bacteria to investigate its antibacterial and tissue regeneration effects. Figure 8 illustrates the healing process (Fig. 8A) and outcomes (Fig. 8, B to M) of superficial skin wounds under various treatments, including (I) PBS (control), (II) NFLA/CuS, (III) AA/NO_2^-, (IV) NFLA/CuS + AA/NO_2^-, (V) NFLA/CuS + NIR, and (VI) NFLA/CuS + AA/NO_2^- + NIR. Wound monitoring and size measurements were conducted on days 0, 3, 7, 10, and 14 after surgery. On day 7, compared to that of the other groups, group VI, with NFLA/CuS + AA/NO_2^- + NIR treatment,

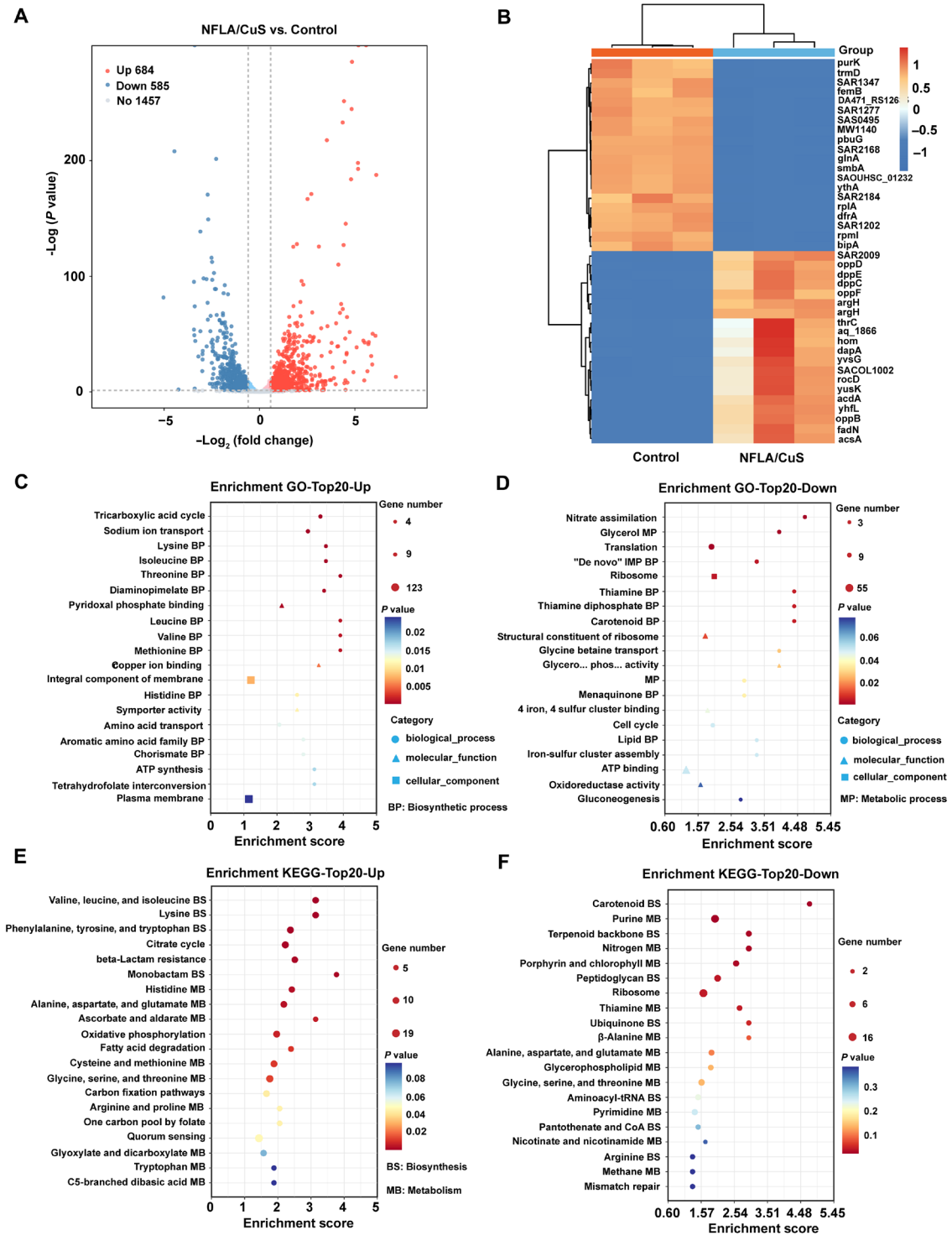

Fig. 6. Transcriptome analysis of MRSA after PBS or NFLA/CuS + AA/NO_2^- treatment. (**A**) Volcano plot of DEGs. The blue dots and red dots represent downregulated and upregulated DEGs, respectively; the gray dots represent undifferentiated expressed genes. (**B**) Cluster analysis of top 20 genes in up-regulated and down-regulated DEGs. Each column represents a sample, and each row represents a gene. Heatmap values represent relative expression levels. (**C**) GO enrichment analysis of the upregulated DEGs. (**D**) GO enrichment analysis of down-regulated DEGs. (**E**) KEGG enrichment analysis of up-regulated DEGs. (**F**) KEGG enrichment analysis of down-regulated DEGs.

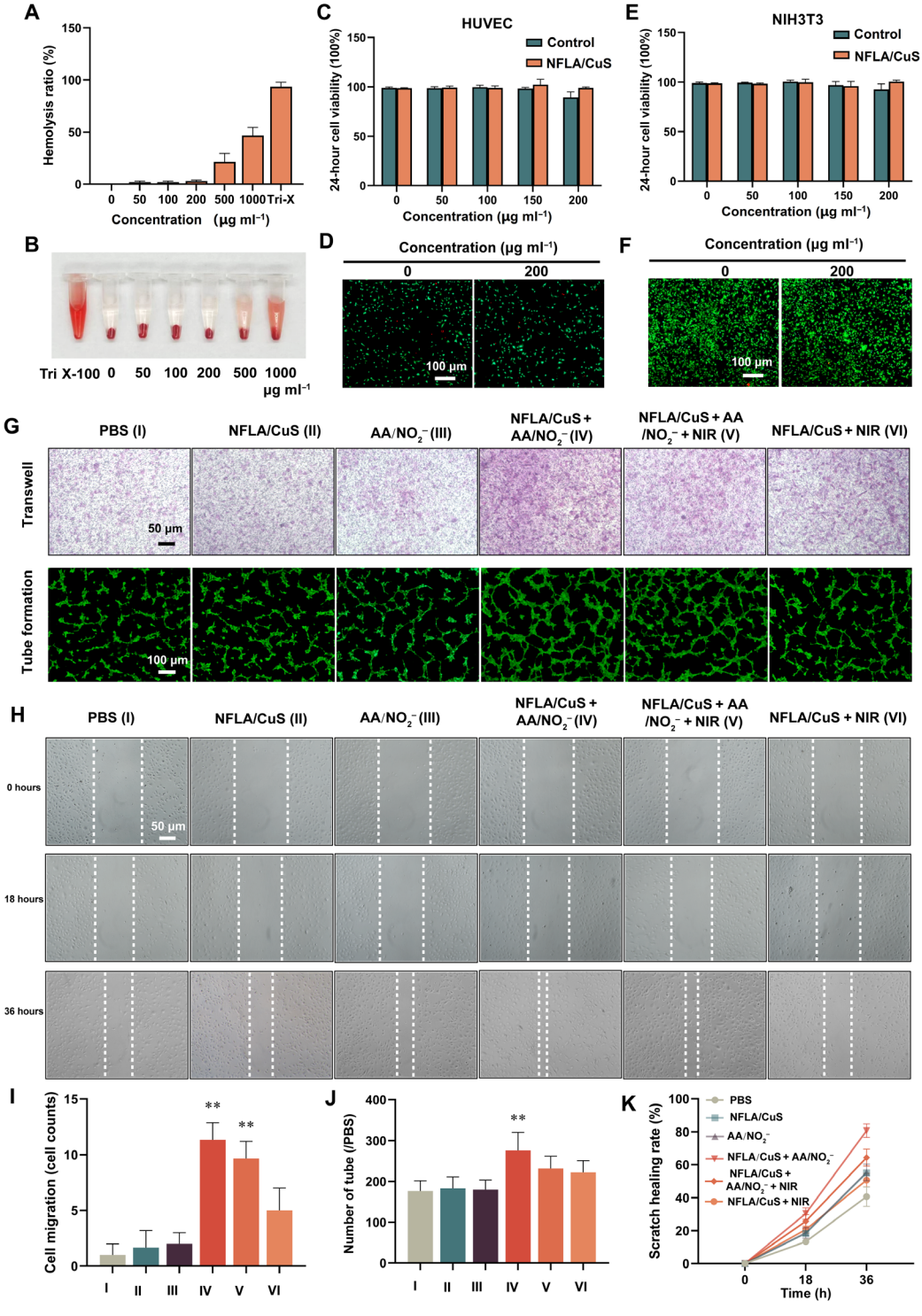

Fig. 7. Cytocompatibility, hemocompatibility of NFLA/CuS NHs and angiogenic effects with different treatments. (**A**) Hemolysis rate of NFLA/CuS NHs. (**B**) Photographs of hemolysis at different NFLA/CuS NHs concentrations. (**C**) Cell viability HUVECs after 24-hour incubation with different concentrations of NFLA/CuS. (**D**) LIVE/DEAD staining of HUVECs after 24-hour incubation with different concentrations of NFLA/CuS, and both images in (D) are the same size with the same scale bar. (**E**) Cell viability of NIH3T3 cells cultured with different concentrations of NFLA/CuS for 24 hours. (**F**) LIVE/DEAD staining of NIH3T3 cells cultured with different concentrations of NFLA/CuS for 24 hours, and both images in (F) are the same size with the same scale bar. (**G**) Transwell migration and tube formation experiments of HUVECs after co-culture with NFLA/CuS NHs in the presence or absence of AA and NO_2^-, and all the images in Transwell group are the same size with the same scale bar of 50 μm but in tube formation with the same scale bar of 100 μm. (**H**) Images of scratch assay of HUVECs cells after different treatments for distinct times (18 and 36 hours), and all the images are the same size with the same scale bar of 50 μm. (**I**) Number of transwell migrated cells counted. (**J**) Tube formation (tube number/PBS) of HUVECs. (**K**) Healing rate of cell scratches after 36 hours. ($n = 6$; $^{**}P < 0.01$).

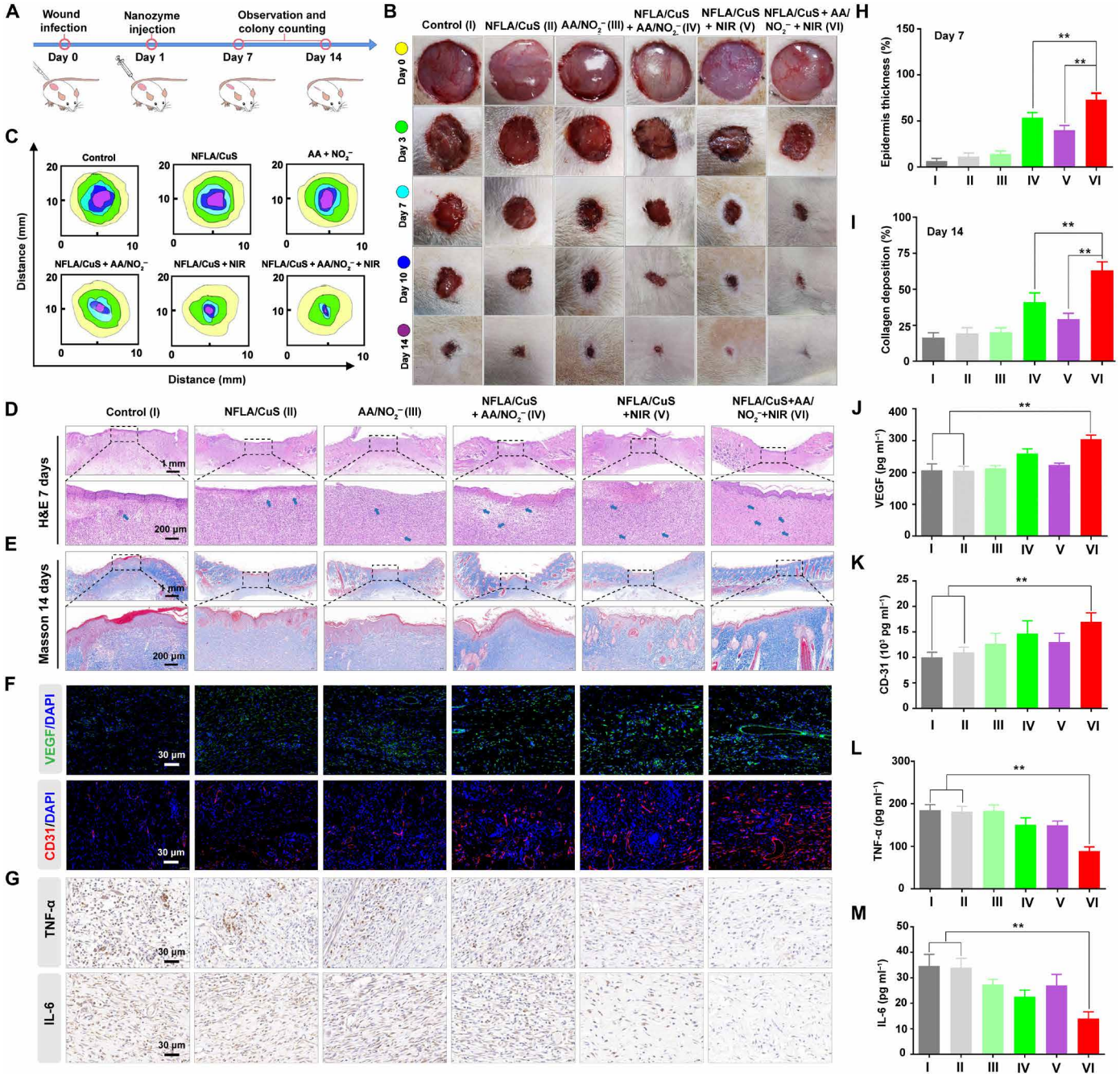

Fig. 8. Therapeutic effect on a rat wound model of MRSA infection with different treatments. (**A**) Construction of the wound infection model and related treatment process. (**B**) Photographs of infected wounds after different treatments: Control (I), NFLA/CuS (II), AA/NO_2^- (III), NFLA/CuS + AA/NO_2^- (IV), NFLA/CuS + NIR (V) and NFLA/CuS + AA/NO_2^- + NIR (VI). (**C**) Schematic diagram of the dynamic wound trajectories of different treatment groups. (**D**) H&E staining of wound tissues from the different treatment groups on day 7, and all the images are the same size with the same scale bar of 1 mm, with the magnified ones of 200 μm. (**E**) Masson staining of wound tissue from the different treatment groups on day 14, and all the images are the same size with the same scale bar of 1 mm, with the magnified ones of 200 μm. (**F**) Immunohistofluorescence staining of VEGF and CD31 after 7 days of treatment, and all the images are the same size with the same scale bar of 30 μm. (**G**) Immunohistochemical staining analysis of TNF-α and IL-6 after 7 days of treatment, and all the images are the same size with the same scale bar of 30 μm. (**H**) Quantification of epidermal thickness. (**I**) Quantification of collagen deposition in the wound tissue. (**J**) Expression level of VEGF. (**K**) Expression level of CD31. (**L**) Expression level of TNF-α. (**M**) Expression level of IL-6. ($n = 6$; $^{**}P < 0.01$). DAPI, 4′,6-diamidino-2-phenylindole.

exhibited a notably reduced wound size (Fig. 8, B and C, and fig. S24). This can be buted to its maximum decrease in residual bacteria (fig. S25) due to the remarkably enhanced NO release stimulated by NIR irradiation at initial stage of CuNIR-mimicking catalysis, as illustrated by the photothermal images showing obvious temperature elevation localized the wound surfaces (fig. S26). Hematoxylin and eosin (H&E) and Masson staining (Fig. 8, D and E, and fig. S27) further revealed obviously reduced inflammatory cells, increased epidermal thickness (Fig. 8H) and collagen deposition (Fig. 8I) in group VI, which were intensified on day 14, indicating an enhanced tissue healing rate. Moreover, immunohistochemical staining (Fig. 8, F and G) displayed an obvious decrease in the expression of interleukin-6 (IL-6) and tumor necrosis factor–α (TNF-α), along with enhanced expression of angiogenesis markers [vascular endothelial growth factor (VEGF) and CD31] in groups IV and VI (NFLA/CuS + AA/NO_2^- and NFLA/CuS + AA/NO_2^- + NIR), which exhibit sustainable low-concentration NO release. These results are consistent with the enzyme-linked immunosorbent assay (ELISA) results (Fig. 8, J to M). Furthermore, the histologic analysis of major tissues (including the heart, liver, spleen, lung, and kidney) (fig. S28) demonstrated the good biocompatibility and biosafety of NFLA/CuS NHs. These findings confirm the high IME adaptability of NFLA/CuS NHs, which are capable of initially suppressing bacterial invasion and inflammation and then promoting neovascularization and collagen deposition, ultimately facilitating the repair of chronically infected wounds.

DISCUSSION

Together, these findings in this work suggest that NFLA/CuS NHs have a superior ability to promote the healing of infected wounds, which can be attributed to the following factors: (i) the elaborate design of CuNIR mimics with multiple copper active sites integrated and immobilized on lysosome fibers, (ii) dynamic and dramatic temporal regulation of NO release rate to adapt to the IME for initial bacterial killing and subsequent and tissue regeneration due to the specific structural contribution in the catalytic reaction, and (iii) excellent biocompatibility. This system we constructed sheds light on the precise design of enzyme mimics in a desired and controlled manner and shows potential for the treatment of skin infections caused primarily by bacteria and chronic infected wounds.

MATERIALS AND METHODS

Preparation of NFLA/CuS NHs

Lysozyme monomer (Shanghai Aladdin Bio-Chem Technology Co., Ltd.) (0.005 g) was first added to a mixture prepared by 4.5 ml of hydrochloric acid (Sinopharm Chemical Reagent Co., Ltd.) (1 M)–glycine (0.007 g) solution and 0.5 ml of acetic acid (1 mM)–choline chloride (Sinopharm Chemical Reagent Co., Ltd.) (0.035 g) solution, which was incubated at 70°C for 5 hours. After twice centrifugation and redispersion, ultrafine NFLA aqueous solution was obtained. Subsequently, 5 ml of $CuCl_2$ (Sinopharm Chemical Reagent Co. Ltd.) aqueous solution was added in 5 ml of NFLA solution at 60°C for 20 min, followed by 5 ml of NaS (Shanghai Aladdin Bio-Chem Technology Co. Ltd.) aqueous solution with the same concentration to Cu^{2+} ions. After further reacting for 2 hours, different NFLA/CuS NHs with CuS/lysozyme mass ratios of 0:1, 0.5/1, 1:1, 3:1, and 6:1 could be obtained by altering the concentration of $CuCl_2$ and NaS aqueous solution.

Characterizations of NFLA/CuS NHs

The morphology of NFLA/CuS NHs was determined by TEM (Tecnai G2 F30), AC-HAADF-STEM (FEI), and atomic force microscopy (AFM) (MultiMode VIII SPM, Bruker). The crystal structure, composition, and chemical state of NFLA/CuS NHs were measured by XRD (Bruker) and XPS (ESCALAB 250). The Cu contents were determined by using the coupled plasma optimal emission spectrometer (VISTA-MPX). UV-visible absorbance spectra were obtained by using a UV-1601 spectrophotometer. The zeta potential and particle size of NFLA/CuS NHs were measured with Zetasizer Nano-ZS (Malvern Instruments, UK).

Catalytic reduction of nitrite

A 1 ml of NFLA/CuS NHs aqueous solution (0.1 mg ml^{-1}) was first added in 5-ml flask, followed by 1 ml of AA aqueous solution (5 mM). When 1 ml of $NaNO_2$ aqueous solution (5 mM) was added into the above mixture, the catalytic reaction began along with bubbling due to NO production. It could be confirmed by $FeSO_4$ chromogenic reaction (*24*) with the procedure shown in fig. S6 and EPR spectrometer with PTIO as a probe. The nitrite concentration was monitored by NED colorimetric method with an absorbance band at 544 nm. On the basis of the nitrite concentration variation, the nitrite conversion and NO generation rate could be calculated. The catalytic performances of $CuCl_2$, CuO, Cu_2O, and CuS (0.1 mg ml^{-1}) followed similar procedure. By detecting nitrite concentration [S] after reacting for 10 s at different initial AA or $NaNO_2$ concentration (1 to 10 mM), the initial reaction rate could be calculated. Michaelis-Menten constant is calculated by the following formula: $1/\nu = K_m/V_{max}[S] + 1/V_{max}$, where ν is the initial velocity, K_m is the Michaelis constant, $[S]$ is the substrate concentration, and V_{max} is the maximum reaction velocity. Temperature and pH-dependent assay were carried out in buffer solutions with pH range of 3.0 to 8.0 and at temperature range of 15° to 60°C, respectively. The effects of AA (2.5 to 10 mM), NO_2^- (2.5 to 10 mM), and NFLA/CuS NHs (0.05 to 0.4 mg ml^{-1}) concentration on the NO_2^- conversions were also investigated by following similar procedure. All the experiments were replicated three times.

Theoretical simulations

All DFT calculations were conducted using the Vienna Ab-initio Simulation Package. Electron-ion interactions were described using projected augmented wave potentials, while exchange-correlation interactions were calculated using Perdew-Burke-Enzerhof pseudopotentials within the framework of generalized gradient approximation. The plane-wave energy cutoff was set to 480 eV. Convergence thresholds were defined as 1.0×10^{-4} eV for energy and 0.02 eV/Å for force. Brillouin zone sampling was performed using $2 \times 2 \times 1$ *k*-points. In addition, a vacuum space of 15 Å was inserted in the *z* direction to prevent interactions between periodic images. All MD simulations were conducted using GROMACS 2020. The lipid membrane and water molecules were modeled using the GROMOS96 53a6 force field and the simple point-charge water model, respectively. Periodic boundary conditions were appᵢied in all directions. The NPT ensemble, with a temperature (T) of 298 K and pressure (P) of 1 bar, was used, with pressure regulation achieved using a Berendsen barostat and temperature control through a velocity-rescale thermostat. Long-range electrostatic interactions were computed using the particle mesh Ewald method. Cutoff distances for van der Waals and electrostatic interactions were set to

1.2 nm. The visualization of snapshots was facilitated using the visual MDs program.

In vitro catalytic antibacterial assays

Bacteria (*E. coli* [American Type Culture Collection (ATCC) 25922] and MRSA (ATCC 33591)] supplied from BioSci (Hangzhou, China) were first resuspended and diluted in PBS (10 mM, pH = 7.4) with an optical density of 0.1 at 600 nm ($OD_{600} = 0.1$). Then, 20 μl of bacterial suspension was added into six different groups of reaction solution (180 μl), (I) PBS, (II) NFLA/CuS, (III) AA/NO_2^-, (IV) NFLA/CuS + AA/NO_2^-, (V) NFLA/CuS + NIR (980 nm, 0.8 W cm^{-2}), and (VI) NFLA/CuS + AA/NO_2^- + NIR, respectively. The final concentrations of NFLA/CuS, AA, and NO_2^- were 50 μg ml^{-1}, 5 mM, and 5 mM, respectively. After reacting for 10 min, the solution was diluted and transferred to LB solid medium, incubating for 24 hours at 37°C. The bacterial viability was determined by calculating the number of bacterial colonies. All experiments were tested in triplicate. The morphologies of bacteria treated under different conditions were observed using SEM and TEM. After sterilization, bacteria were separated by centrifugation at 4000 rpm and fixed in 400 μl of 2.5% glutaraldehyde fixative (pH = 7.3), subsequently subjected to graded dehydration with ethanol. Last, concentrated bacteria were dropped onto a silicon wafer surface and observed using SEM or onto copper grid and observed using TEM. Further observation of bacterial death proportions was performed using the LIVE/DEAD staining method with the Thermo Fisher LIVE/DEAD BacLight Bacterial Viability Kit (L7012), which consists of SYTO9 and propidium iodide as dyes. Intracellular ROS levels was measured by a multidetection microplate reader using the most commonly used and most sensitive 7-dichlorofuorescin diacetate (DCFH-DA) as a probe, which can penetrate into cell and decompose into DA and DCFH. DCFH cannot pass through the cell membrane and has an excitation wavelength of 488 nm and an emission wavelength of 525 nm after being oxidized by ROS.

Transcriptome analysis

MRSA was subjected to treatment with PBS as a control, and a mixture consisting of NFLA/CuS NHs (50 μg ml^{-1}), AA (5 mM), and sodium nitrite (5 mM) in PBS at pH 5.5 for 20 min. Following treatment, bacterial precipitates were collected via centrifugation. Total RNA extraction from MRSA was conducted using an RNA extraction kit following the manufacturer's protocol. RNA purity and quantification were determined using a NanoDrop 2000 spectrophotometer, while RNA integrity was assessed using the Agilent 2100 Bioanalyzer. Subsequently, libraries were prepared using the VAHTS Universal V6 RNA-seq Library Prep Kit according to the manufacturer's instructions. Transcriptome sequencing and analysis were performed by OE Biotech Co. Ltd. (Shanghai, China). Three independent assays were conducted for each experimental group. Libraries were sequenced on an Illumina NovaSeq 6000 platform, generating 150–base pair paired-end reads. Clean reads were aligned to the reference genome using HISAT2. Fragments Per Kilobase Million values for each gene were calculated, and read counts for each gene were obtained using HTSeq-count. Principal components analysis was carried out using R (v 3.2.0) to assess sample biological duplication. Differential expression analysis was conducted using DESeq2, with a threshold set at q value < 0.05 and fold change > 2 or fold change < 0.5 for significantly DEGs. Enrichment analysis of DEGs—including GO, KEGG pathway, Reactome, and WikiPathways—was performed using R (v 3.2.0) based on hypergeometric distribution. In addition, Gene Set Enrichment Analysis (GSEA) was performed using GSEA software.

Biocompatibility of NFLA/CuS NHs in vitro

To assess the toxic effects of NFLA/CuS NHs, a CCK-8 assay was used. Briefly, HUVECs (BNCC342387) and NIH-3 T3 cells (BNCC100843) were provided by BNCC (Shangcheng, China). The cells (1×10^4 cells per well) were plated onto 24-well plates in triplicate and then cocultured with various concentrations (0 to 200 μg ml^{-1}) of NFLA/CuS NHs. After 24 hours, CCK-8 reagents were added to each well, and the plates were incubated at 37°C for 2 hours. Cell viability was subsequently determined by measuring the OD_{450} using a microplate reader (BioTek, Vermont, USA).

To evaluate the blood compatibility of NFLA/CuS NHs, a hemolysis activity assay was conducted. Specifically, rat blood (500 μl) was collected and processed at 4°C using a centrifuge at 3500 rpm for 5 min. A clear supernatant was obtained after washing with water. Subsequently, a mixture of various concentrations (0 to 1000 μg ml^{-1}) of NFLA/CuS NHs and 1 ml of erythrocytes was incubated in a tube for 4 hours. Sterile PBS served as the negative control, while pure water was used as the positive control. The upper layer of solution was collected after centrifugation, and absorbance was measured at 545 nm using a microplate reader. All experiments were tested in triplicate.

Transwell cell migration assay

Matrigel matrix gel was diluted with serum-free cell culture medium or PBS at 4°C (on ice). A total of 60 μl of the above mixture was added vertically to the Transwell chamber to evenly coat the bottom and then incubated at 37°C for 1 to 3 hours to polymerize the gel into a thin film. After incubation, excess liquid in the upper chamber was removed, and 100 μl of serum-free medium was added to each well for 30 min to hydrate the basement membrane. A total of 200 μl of cell suspension (2.5×10^5 cells /ml) was added to the upper chamber and incubated at 37°C for 16 hours. The culture medium was removed, the chamber was removed, and the cells in the upper chamber were gently wiped off with a cotton swab and washed with PBS. Subsequently, the cells were fixed with 4% paraformaldehyde, washed three times with PBS solution, stained with 0.1% crystal violet solution for 15 min. The dye was removed, and the cells were washed three times with PBS solution and observed and photographed under a microscope. All experiments were tested in triplicate. ImageJ was used to calculate the migration data.

Scratch assay

Different groups of cells were seeded at a density of 4×10^5 cells per well in six-well plates and cultured at 37°C in a cell culture incubator for 24 hours. When the cell density reached 90%, a scratch was made in the center of each well using the tip of a 200-μl pipette. The culture medium was removed, and the cells were washed with sterile PBS solution to remove cell debris. The medium containing 0.5% serum was replaced, and the cells were continued to be cultured. All experiments were tested in triplicate. Images were captured using an inverted microscope at 0, 18, and 36 hours, and the migration area data were calculated using ImageJ.

Tube formation assay

For the tube formation assay, 24-well plates and 200-μl pipette tips were precooled at −20°C, and Matrigel matrix gel was thawed overnight at 4°C. A total of 100 μl of basement membrane matrix was

added to each well and incubated at 37°C for 30 min to solidify. Subsequently, HUVECs were seeded at a density of 8×10^4 cells per well according to the experimental groups, 500 μl of cell suspension was added, and the cells were cultured in a cell culture incubator. After 4 to 6 hours of culture, the tubes were observed and photographed with an optical microscope, and parameters such as tube count were analyzed and statistically analyzed using ImageJ. All experiments were tested in triplicate.

Wound healing in vivo

To investigate the antibacterial and wound healing properties in vivo, wound models of SD rats were established by making full thickness cutaneous skin wounds. All experimental procedures strictly followed universally recognized guidelines and were approved by the Ethics Committee of Jiangsu University (UJS-IACUC-AP-2023030905). In brief, 36 6-week-old male SD rats (150 to 200 g) (Laboratory Animal Center of Jiangsu University) were housed in a specific pathogen–free environment and randomly divided into six groups. Specifically, the rats were anesthetized with 2.5% pentobarbital sodium (2 ml kg^{-1}), and the dorsal surface of the rats was depilated and disinfected. Then, full thickness wounds were created on the backs of rats, and the diameter was set at 1.5 cm. Infection was induced by placing *MRSA* onto the wounds (200 μl, 10^6 colony-forming units ml^{-1}). The day after infection, the wounds were treated following the protocol for each group, control (I), NFLA/CuS (II), AA/NO_2^- (III), NFLA/CuS + AA/NO_2^- (IV), NFLA/CuS + NIR (V), and NFLA/CuS + AA/NO_2^- + NIR (VI). The photothermal imaging was conducted by an infrared camera (Brit IR, Wuhan Gold Infrared Co., Ltd.). These wounds were observed and snapped to visualize the healing process. After 1 and 2 weeks, three rats were euthanized. The wound tissues were harvested and fixed in 4% paraformaldehyde for subsequent histological analysis, and the numbers of bacteria were evaluated by plate count methods as previously described.

Histology and histomorphometry analysis

After fixation for 48 hour, the histological skin tissues samples were embedded in paraffin. H&E staining was then performed on the sections to assess the local inflammation and calculate the number of infiltrated inflammatory cells. Masson staining was also conducted to evaluate collagen volume fraction. The stained sections were observed and captured with a high-quality light microscope (Zeiss). Histomorphometric analysis was performed by the Image Pro-Plus 6.0 software (Media Cybernetics).

Immunofluorescence histochemistry

After dewaxing, gradient hydration and antigen retrieval, the sections were incubated with rabbit anti–TNF-α (Abclone, A11534), anti–IL-6 (Abclone, A11114), anti-CD31 (Abcam, ab182981), or anti-VEGF (Abcam, ab32152) antibodies in the dark at 4°C for 12 hours. Then, the sections were washed followed by a 2-hour incubation with the proper secondary antibodies at room temperature. The number of positive cells in specific areas was determined by fluorescence microscopy.

Expression of cytokines and growth factors

Regenerated skin tissues were excised on day 7 and analyzed for protein quantification. Expression levels of angiogenic and inflammatory cytokines (VEGF, CD-31, TNF-α, and IL-6) were measured by ELISA kits.

Biosafety evaluation

To detect the biological safety of the material on vital organs, NFLA/CuS NHs were injected under the skin of healthy rats. Biochemical index evaluation of blood samples was performed after 2 weeks of treatment. Specifically, the serum creatine kinase, aspartate transaminase, alanine aminotransferase, blood urea nitrogen, and uric acid levels were detected. In addition, major organs (the liver, spleen, heart, lung, and kidney) were stained with H&E to evaluate biological safety.

Statistical analysis

All data are expressed as the means ± SD. Statistical significance was measured by one-way analysis of variance (ANOVA) with Tukey's post hoc multiple comparison test. A value of $P < 0.05$ was considered significant.

Supplementary Materials

This PDF file includes:

Figs. S1 to S28

Tables S1 and S2

REFERENCES AND NOTES

1. M. Ye, Y. Zhao, Y. Wang, M. Zhao, N. Yodsanit, R. Xie, D. Andes, S. Gong, A dual-responsive antibiotic-loaded nanoparticle specifically binds pathogens and overcomes antimicrobial-resistant infections. *Adv. Mater.* **33**, e2006772 (2021).
2. G. Guo, H. Zhang, H. Shen, C. Zhu, R. He, J. Tang, Y. Wang, X. Jiang, J. Wang, W. Bu, X. Zhang, Space-selective chemodynamic therapy of $CuFe_5O_8$ Nanocubes for Implant-Related infections. *ACS Nano* **14**, 13391–13405 (2020).
3. Y. Feng, F. Chen, J. M. Rosenholm, L. Liu, H. Zhang, Efficient nanozyme engineering for antibacterial therapy. *Mater. Futures* **1**, 023502 (2022).
4. S. Hatz, J. D. C. Lambert, P. R. Ogilby, Measuring the lifetime of singlet oxygen in a single cell: addressing the issue of cell viability. *Photochem. Photobiol. Sci.* **6**, 1106–1116 (2007).
5. B. Halliwell, The antioxidant paradox. *Lancet* **355**, 1179–1180 (2000).
6. M. D. Temple, G. G. Perrone, I. W. Dawes, Complex cellular responses to reactive oxygen species. *Trends Cell Biol.* **15**, 319–326 (2005).
7. B. Zhang, Y. Yang, J. Yi, Z. Zhao, R. Ye, Hyperglycemia modulates M1/M2 macrophage polarization via reactive oxygen species overproduction in ligature-induced periodontitis. *J. Periodontal Res.* **56**, 991–1005 (2021).
8. D. D. Thomas, X. Liu, S. P. Kantrow, J. R. Lancaster Jr., The biological lifetime of nitric oxide: implications for the perivascular dynamics of NO and O_2. *Proc. Natl. Acad. Sci. U.S.A* **98**, 355–360 (2001).
9. S. Yu, G. Li, R. Liu, D. Ma, W. Xue, Dendritic Fe_3O_4@Poly(dopamine)@PAMAM nanocomposite as controllable NO-releasing material: A synergistic photothermal and NO antibacterial study. *Adv. Funct. Mater.* **28**, 1707440 (2018).
10. Z. Shen, S. Zheng, S. Xiao, R. Shen, S. Liu, J. Hu, Red-light-mediated photoredox catalysis enables self-reporting nitric oxide release for efficient antibacterial treatment. *Angew. Chem. Int. Ed. Engl.* **60**, 20452–20460 (2021).
11. C. Opländer, T. Müller, M. Baschin, A. Bozkurt, G. Grieb, J. Windolf, N. Pallua, C. V. Suschek, Characterization of novel nitrite-based nitric oxide generating delivery systems for topical dermal application. *Nitric Oxide* **28**, 24–32 (2013).
12. T.-K. Nguyen, R. Selvanayagam, K. K. K. Ho, R. Chen, S. K. Kutty, S. A. Rice, N. Kumar, N. Barraud, H. T. T. Duong, C. Boyer, Co-delivery of nitric oxide and antibiotic using polymeric nanoparticles. *Chem. Sci.* **7**, 1016–1027 (2016).
13. S. Hematian, M. A. Siegler, K. D. Karlin, Heme/Copper Assembly Mediated Nitrite and Nitric Oxide Interconversion. *J. Am. Chem. Soc.* **134**, 18912–18915 (2012).
14. G. H. Oliveira-Paula, L. C. Pinheiro, J. E. Tanus-Santos, Mechanisms impairing blood pressure responses to nitrite and nitrate. *Nitric Oxide* **85**, 35–43 (2019).
15. L. B. Maia, J. J. G. Moura, How biology handles nitrite. *Chem. Rev.* **114**, 5273–5357 (2014).
16. S. Horrell, D. Kekilli, R. W. Strange, M. A. Hough, Recent structural insights into the function of copper nitrite reductases. *Metallomics* **9**, 1470–1482 (2017).
17. A. K. Nath, C. Ghosh, M. Roy, M. Seal, S. Ghosh Dey, Nitrite reductase activity of heme and copper bound Aβ peptides. *Dalton Trans.* **48**, 7451–7461 (2019).
18. K. K. Konopińska, N. J. Schmidt, A. P. Hunt, N. Lehnert, J. Wu, C. Xi, M. E. Meyerhoff, Comparison of copper(II)–ligand complexes as mediators for preparing electrochemically modulated nitric oxide-releasing catheters. *ACS Appl. Mater. Interfaces* **10**, 25047–25055 (2018).
19. V. Wonoputri, C. Gunawan, S. Liu, N. Barraud, L. H. Yee, M. Lim, R. Amal, Copper complex in poly(vinyl chloride) as a nitric oxide-generating catalyst for the control of nitrifying bacterial biofilms. *ACS Appl. Mater. Interfaces* **7**, 22148–22156 (2015).

20. Y. Feng, H. Wang, J. Zhang, Y. Song, M. Meng, J. Mi, H. Yin, L. Liu, Bioinspired synthesis of Au nanostructures templated from amyloid β peptide assembly with enhanced catalytic activity. *Biomacromolecules* **19**, 2432–2442 (2018).
21. T. Sun, Y. Feng, J. Peng, Y. Hao, L. Zhang, L. Liu, Cofactors-like peptide self-assembly exhibiting the enhanced catalytic activity in the peptide-metal nanocatalysts. *J. Colloid. Interface Sci.* **617**, 511–524 (2022).
22. A. Levin, T. A. Hakala, L. Schnaider, G. J. Bernardes, E. Gazit, T. P. Knowles, Biomimetic peptide self-assembly for functional materials. *Nat. Rev. Chem.* **4**, 615–634 (2020).
23. Y. Feng, Z. Cheng, A.-K. K. Larsen, H. Shi, T. Sun, P. Zhang, M. Dong, L. Liu, Amyloid-like nanofibrous network confined and aligned ultrafine bimetallic nanozymes for smart antibacterial therapy. *Mater. Today Bio* **22**, 100730 (2023).
24. H. I. Schlesinger, A. Salathe, Absorption spectra of nitrosylsulfuric acid and of the complex compounds of copper sulfate and of ferrous sulfate with nitric oxide[2,3]. *J. Am. Chem. Soc.* **45**, 1863–1878 (1923).
25. Y. Duan, Y. Wang, X. Li, G. Zhang, G. Zhang, J. Hu, Light-triggered nitric oxide (NO) release from photoresponsive polymersomes for corneal wound healing. *Chem. Sci.* **11**, 186–194 (2020).
26. S. Ghosh, A. Dey, Y. Sun, C. P. Scholes, E. I. Solomon, Spectroscopic and computational studies of nitrite reductase: Proton induced electron transfer and backbonding contributions to reactivity. *J. Am. Chem. Soc.* **131**, 277–288 (2009).
27. G. Cioncoloni, I. Roger, P. S. Wheatley, C. Wilson, R. E. Morris, S. Sproules, M. D. Symes, Proton-coupled electron transfer enhances the electrocatalytic reduction of nitrite to NO in a bioinspired copper complex. *ACS Catal.* **8**, 5070–5084 (2018).
28. Q. Liu, K. Wan, Y. Shang, Z.-G. Wang, Y. Zhang, L. Dai, C. Wang, H. Wang, X. Shi, D. Liu, B. Ding, Cofactor-free oxidase-mimetic nanomaterials from self-assembled histidine-rich peptides. *Nat. Mater.* **20**, 395–402 (2021).
29. Y. Fan, X.-D. Li, P.-P. He, X.-X. Hu, K. Zhang, J.-Q. Fan, P.-P. Yang, H.-Y. Zheng, W. Tian, Z.-M. Chen, L. Ji, H. Wang, L. Wang, A biomimetic peptide recognizes and traps bacteria in vivo as human defensin-6. *Sci. Adv.* **6**, eaaz4767 (2020).
30. S. Poudel, H. Tsunemoto, Y. Seif, A. V. Sastry, R. Szubin, S. Xu, H. Machado, C. A. Olson, A. Anand, J. Pogliano, V. Nizet, B. O. Palsson, Revealing 29 sets of independently modulated genes in Staphylococcus aureus, their regulators, and role in key physiological response. *Proc. Natl. Acad. Sci. U.S.A.* **117**, 17228–17239 (2020).
31. N. Häffner, J. Bär, V. Dengler Haunreiter, S. Mairpady Shambat, K. Seidl, H. A. Crosby, A. R. Horswill, A. S. Zinkernagel, Intracellular environment and agr system affect colony size heterogeneity of *Staphylococcus aureus*. *Front. Microbiol.* **11**, 1415 (2020).
32. C. Kohler, S. Wolff, D. Albrecht, S. Fuchs, D. Becher, K. Büttner, S. Engelmann, M. Hecker, Proteome analyses of Staphylococcus aureus in growing and non-growing cells: a physiological approach. *Int. J. Med. Microbiol.* **295**, 547–565 (2005).
33. M. Liebeke, K. Dörries, D. Zühlke, J. Bernhardt, S. Fuchs, J. Pane-Farre, S. Engelmann, U. Völker, R. Bode, T. Dandekar, A metabolomics and proteomics study of the adaptation of Staphylococcus aureus to glucose starvation. *Mol. Biosyst.* **7**, 1241–1253 (2011).
34. C. Li, N. Chen, X. Zhang, K. Shahzad, R. Qi, Z. Zhang, Z. Lu, Y. Lu, X. Yu, M. H. Zafar, M. Wang, W. Liu, Mixed silage with Chinese cabbage waste enhances antioxidant ability by increasing ascorbate and aldarate metabolism through rumen Prevotellaceae UCG-004 in Hu sheep. *Front. Microbiol.* **13**, 978940 (2022).
35. S. J. Gabryszewski, T. W. F. Lung, M. K. Annavajhala, K. L. Tomlinson, S. A. Riquelme, I. N. Khan, L. P. Noguera, M. Wickersham, A. Zhao, A. M. Mulenos, Metabolic adaptation in methicillin-resistant Staphylococcus aureus pneumonia. *Am. J. Respir. Cell Mol. Biol.* **61**, 185–197 (2019).
36. J. E. Choby, L. A. Mike, A. A. Mashruwala, B. F. Dutter, P. M. Dunman, G. A. Sulikowski, J. M. Boyd, E. P. Skaar, A small-molecule inhibitor of iron-sulfur cluster assembly uncovers a link between virulence regulation and metabolism in Staphylococcus aureus. *Cell Chem. Biol.* **23**, 1351–1361 (2016).
37. C. A. Roberts, H. M. Al-Tameemi, A. A. Mashruwala, Z. Rosario-Cruz, U. Chauhan, W. E. Sause, V. J. Torres, W. J. Belden, J. M. Boyd, The Suf iron-sulfur cluster biosynthetic system is essential in Staphylococcus aureus, and decreased Suf function results in global metabolic defects and reduced survival in human neutrophils. *Infect. Immun.* **85**, e00100–e00117 (2017).
38. F. Zhang, Q. Zhang, X. Li, N. Huang, X. Zhao, Z. Yang, Mussel-inspired dopamine-CuII coatings for sustained in situ generation of nitric oxide for prevention of stent thrombosis and restenosis. *Biomaterials* **194**, 117–129 (2019).
39. Y. Chen, P. Gao, L. Huang, X. Tan, N. Zhou, T. Yang, H. Qiu, X. Dai, S. Michael, Q. Tu, N. Huang, Z. Guo, J. Zhou, Z. Yang, H. Wu, A tough nitric oxide-eluting hydrogel coating suppresses neointimal hyperplasia on vascular stent. *Nat. Commun.* **12**, 7079 (2021).

Acknowledgments

Funding: We acknowledge the financial support from National Natural Science Foundation of China (nos. 32371407, 22072060, and 82160421) and Natural Science Foundation of Jiangsu Province (no. BK20211322). This work is also supported by Changzhou Sci&Tech Program (CJ20230069) and Top Talent of Changzhou "The14th Five-Year Plan" High-Level Health Talents Training Project (CZQM2021012). **Author contributions:** Conceptualization: Y.F. and L.L. Methodology: Y.F. and T.Y. Investigation: Y.Y. and H.S. Visualization: Y.F. and Y.Y. Supervision: L.W. and L.L. Writing—original draft: Y.F. and L.W. Writing—review and editing: J.B. and L.L. **Competing interests:** The other authors declare that they have no competing interests. **Data and materials availability:** All data needed to evaluate the conclusions in the paper are present in the paper and/or the Supplementary Materials.

Submitted 3 April 2024
Accepted 26 July 2024
Published 30 August 2024
10.1126/sciadv.adp5935